Magnetic Proximity Effect in Graphene/$CrBr_3$ van der Waals Heterostructures

*Chaolong Tang, Zhaowei Zhang, Shen Lai, Qinghai Tan, Wei-bo Gao**

Dr. C. Tang, Z. Zhang, Dr. S. Lai, Dr. Q. Tan, Prof. W. Gao
Division of Physics and Applied Physics
School of Physical and Mathematical Sciences
Nanyang Technological University
Singapore 637371, Singapore
E-mail: wbgao@ntu.edu.sg

Prof. W. Gao
The Photonics Institute and Centre for Disruptive Photonic Technologies
Nanyang Technological University
Singapore 637371, Singapore

Keywords: magnetic proximity effect, graphene, $CrBr_3$, van der Waals, Zeeman spin Hall effect

Two-dimensional (2D) van der Waals heterostructures serve as a promising platform to exploit various physical phenomena in a diverse range of novel spintronic device applications. The efficient spin injection is the prerequisite for these devices. The recent discovery of magnetic 2D materials leads to the possibility of fully 2D van der Waals spintronics devices by implementing spin injection through magnetic proximity effect (MPE). Here, the investigation of magnetic proximity effect in 2D graphene/$CrBr_3$ van der Waals heterostructures is reported, which is probed by Zeeman spin Hall effect through non-local measurements. Quantitative estimation of Zeeman splitting field demonstrates a significant magnetic proximity exchange field even in a low magnetic field. Furthermore, the observed anomalous longitudinal resistance changes at the Dirac point $R_{XX,D}$ with increasing magnetic field near $\nu = 0$ may attribute to the MPE induced new ground state phases. This MPE revealed in our graphene/$CrBr_3$ van der Waals heterostructures therefore provides a solid physics basis and key functionality for next generation 2D spin logic and memory devices.

The exploration of the spin degree of freedom holds promise for next-generation memory and logic devices[1,2]. These devices use spins to carry information instead of charges and therefore can lead to low-power, high-speed operations[3] Graphene provides an interesting platform for spintronics with the unique advantages of a long spin lifetime and long spin transport distance[4,5]. For spintronic devices, spin initialization is a prerequisite. There are three main methods for spin injection in graphene[6]. First, conducting ferromagnetic electrodes directly on graphene can lead to efficient spin injection. However, it suffers from the drawback of naturally short-circuit the graphene layer and restrict the design of spin switches. Second, magnetic dopants can be introduced into graphene. It can lead to the degradation of its unique property of high carrier mobility. Therefore, a lot of efforts have been devoted to the third method, that is, the introduction of magnetism in graphene with the proximity effect in the interface of magnetic insulators and graphene. Pioneer works have been demonstrated with 3D bulk magnetic insulators like yttrium iron garnet, Europium (II) sulfide and bismuth ferrite[7-14].

Due to the short-range nature of the magnetic exchange coupling, a fully 2D van der Waals heterostructures is desired for downsizing the device and introducing magnetic proximity effect (MPE) at the same time. The recent profound discoveries of 2D ferromagnets[15-28] bring the possibility of 2D ferromagnetic van der Waals heterostructures[29-35], it is urgent and essential to comprehensively investigate the magnetic coupling between graphene and 2D ferromagnetic materials for developing 2D spintronic devices. Not just evidence the existence of MPE in 2D ferromagnetic van der Waals heterostructures[36-37], here, we report the direct observation of MPE in graphene/$CrBr_3$ van der Waals heterostructures by probing Zeeman spin Hall effect through non-local transport measurements, a further quantitative estimation of Zeeman splitting field demonstrates a significant magnetic proximity exchange field even in a low magnetic field. Furthermore, we observe anomalous longitudinal resistance changes at the Dirac point $R_{XX,D}$ with increasing external magnetic field near $\nu = 0$. This may attribute to the MPE induced

ground state phases transformation of graphene from the ferromagnetic state at the lower magnetic field and a canted antiferromagnetic state at a higher field in quantum Hall regime.

A typical graphene/$CrBr_3$ van der Waals heterostructure with Hall bar structure for electrical transport measurement is fabricated as shown in **Figure 1**a. In order to reach the best performance and a substantial MPE in graphene/$CrBr_3$ heterostructures, we optimize the fabrication process and conditions to achieve the desired heterostructures (see experimental section for details). The sample in the final stage is encapsulated and protected by PMMA, which keeps the device surface away from the moisture and air for cryotemperature tests. The atomic structure of layered $CrBr_3$ is shown in Figure 1b. The Cr^{3+} ions are configured in a honeycomb network, and the green arrows represent the spin direction of Cr atoms, which are found to exhibit a strong ferromagnetic coupling[38-43]. The Raman spectra of Figure 1c indicates the monolayer graphene still preserves a high crystal quality when heterostructured with $CrBr_3$ layer. The optical image in Figure 1d displays the as-fabricated graphene/$CrBr_3$ heterostructures, along with the H-shape Hall bar structure for conducting non-local measurements.

As shown in **Figure 2**a, with the Zeeman effect, the splitting of the Dirac cone in graphene generates electron- and hole-like carriers with opposite spins near the Dirac point. This property can induce Zeeman spin Hall effect, with the working principle shown in Figure 2b. First, a source-drain current I is applied in the presence of an external perpendicular magnetic field, because the Lorentz force has opposite signs for electrons and holes, the net charge current is zero and hence no net transverse charge current is produced in the sample. However, the net spin current is nonzero (Figure 2b). With this configuration, a non-local voltage V_{nl} can be measured in the remote regions[44]. With a larger magnetic field, we expect to observe a larger V_{nl}. Therefore, we could probe the MPE in graphene/$CrBr_3$ heterostructures via the V_{nl} induced by Zeeman spin Hall effect (ZSHE) in graphene layer.

The observation of MPE in graphene/$CrBr_3$ heterostructures through ZSHE is shown in Figure 2c,d. The acquired non-local resistances $R_{nl} = V_{nl}/I$ as a function of the back-gate bias V_g

under a series of external fields at temperature of 2 K are plotted in Figure 2c. The R_{nl} peak at the Dirac point is written as $R_{nl,D}$. Along with the external magnetic field increasing, the non-local resistance $R_{nl,D}$ rises sharply, suggesting a distinct Zeeman splitting energy enhancement. Moreover, other possible source of producing non-local signal like Ohmic contribution were analyzed and excluded (Figure S5, Supporting Information). As to the finite V_{nl} at 0 T, it may be due to the spin Hall effect caused by spin polarization which is induced by the exchange field under 0 T[13,43]. In order to confirm the origin of this Zeeman splitting energy enhancement resulting from the MPE, we further measured the temperature dependence of $R_{nl,D}$. Figure 2d indicates that $R_{nl,D}$ in graphene/$CrBr_3$ heterostructures experiences an abrupt slowdown as the temperature exceeds at about 37 K, corresponding to the transition temperature T_C of $CrBr_3$ which has a phase change from ferromagnetic to paramagnetic state. In contrast, pure graphene shows a very weak temperature dependence without distinguishable onset feature like graphene/$CrBr_3$ heterostructures. Undoubtedly, we can therefore conclude that the MPE is the dominating contribution to induce $R_{nl,D}$ in graphene/$CrBr_3$ heterostructures when the temperature is lower than the T_C of $CrBr_3$.

Using as described Zeeman spin Hall probing, magnetic field dependence measurement and related theoretical calculation of the magnetic field induced Zeeman splitting energy in graphene/$CrBr_3$ could provide quantitative information on MPE in the 2D van der Waals heterostructures. **Figure 3**a is the plot of $R_{nl,D}$ changes (data were divided by $R_{nl,D}$(0 T) for comparison purpose) with external magnetic field sweep measured at 2 K. It can be observed that $R_{nl,D}$ of graphene/$CrBr_3$ heterostructures reaches orders-of-magnitude increase with respect to the magnetic field from 0 to 4 T comparing with pristine graphene. Inset curve is the measured R_{nl} of heterostructures as a function of V_{g} under 4 T. The quantitative description of MPE in graphene/$CrBr_3$ heterostructures can be estimated by calculating its Zeeman splitting energy E_Z and the total Zeeman field B_Z. We firstly adopt the definition of R_{nl} as follows[44-47]

$$R_{nl} \equiv \frac{dV_{nl}}{dI} \propto \frac{1}{\rho_{xx}} \left(\frac{\partial \rho_{xy}}{\partial \mu} E_Z\right)^2 \quad (1)$$

where ρ_{xx} and ρ_{xy} is the longitudinal and Hall resistivity, respectively, both are strongly depending on the external out of plane magnetic field ($B_\perp$); μ is the chemical potential, E_Z is the Zeeman splitting energy which is proportional to the total external field (B). Therefore, we have $R_{nl} = \beta(B_\perp)B^2$, β represents the ρ_{xx} and ρ_{xy} manifested parameters. The R_{nl} peak at the Dirac point $R_{nl,D}$ could be further written as $R_{nl} = R_0 + \beta(B_\perp)E_Z^2$, R_0 stands for the non-local resistance of non ZSHE signal at zero field. Moreover, the $E_Z = g\mu_B B_Z = g\mu_B(B_{MPE} + B(\mu_0 H))$can be further written as (Text S1, Supporting Information)

$$E_Z = E_{Z0} \cdot \frac{\sqrt{(1+\mu_*^2 B^2)B_0^2}}{\sqrt{(1+\mu_*^2 B_0^2)B^2}} \cdot \frac{\sqrt{R_{nl,D}(B) - R_0}}{\sqrt{R_{nl,D}(B_0) - R_0}} \quad (2)$$

where μ_* is the carrier mobility, B_0 is the zero magnetic field, B_{MPE} represents the field induced by MPE in graphene/$CrBr_3$ heterostructures. For the convenience of calculating E_Z, we have an approximation of $E_{Z0} \approx g\mu_B B_0$ by neglecting the MPE field contribution and using B_0 = 0.1 T as reference magnetic field to estimate the lower-bound of E_Z[12]. The calculated Zeeman splitting energy E_Z and its corresponding Zeeman field B_Z are plotted against the external magnetic field in Figure 3b, respectively. The inset provides field effect mobility[48,49] (μ_*) versus carrier density of graphene/$CrBr_3$ heterostructures, high carrier mobility ensures the excellent device performance of 2D magnetic coupling and further observation of pronounced quantum oscillations. Figure 3b shows a clear evidence of the substantial magnetic exchange field by presenting two little different slopes of line segments as well as the magnetic field increasing. Since the magnetic exchange field is nearly irrelevant to the external field $B_\perp$,when the applied field is low and less than about 1 T, the line slope is a bit steeper than the one with field larger than 1 T, which demonstrates that magnetic exchange field is the dominating contribution to the nonlocal resistance at low field. Giving $\mu_0 H$ = 4 T, the estimate B_Z is approximately twice of applied field, which seems weaker than other reported 2D or

graphene/ferromagnetic material systems like WSe_2/EuS[50], Graphene/EuS[12] and Graphene/ $BiFeO_3$[13], but this result is reasonable, because 2D $Crbr_3$ has a smaller interlayer exchange coupling energy J = 1.56 meV[51], and its magnetic moment per Cr ion is 3.25 μ_B[52], comparing with EuS which has an exchange coupling energy J ~10 meV, and the magnetic moment per Eu ion is 7.9 μ_B[53].

As shown in **Figure 4**, four-probe longitudinal resistivity measurement further reveals the MPE effect in the quantum Hall regime of graphene/$CrBr_3$ heterostructures, which not only lifts the ground state degeneracy of graphene but also indicates the ground state phase transformation near ν = 0 in the quantum Hall regime. Color map of Figure 4a shows a typical Landau Fan of the longitudinal resistance R_{XX} as a function of the gate bias V_{g} and the applied magnetic field $B(\mu_0 H)$. Similar to the quantum mobility measurement of graphene in previous report[54], the central bright region near the Dirac point suggests that a gap is opened when the magnetic field is larger than 5 T. We further extract longitudinal resistance measured under external field from 2 to 9 T as shown in Figure 4b. For clarity of labelling the Landau level filling factors, resistance curves are vertically shifted and are proportional to the applied magnetic field. The filling factor ν of the Landau level can be obtained by using $\nu = \pm 4(|n|+1/2)$ where n = 0, 1, 2 … is the Landau level index. As shown in Figure 4c, ν can be directly derived from the longitudinal resistivity versus gate bias curve at each local R_{XX} minimum, which shows pronounced quantum oscillations. Inset figure manifests that V_{g} is linearly proportional to each ν value, as expected. Since the injected carriers by gate voltage into graphene could be expressed with e^2B/h, we could therefore use capacitance model[13] to calculate the gate voltage $(V_g - V_D)$ or the corresponding electron density with magnetic field at $\nu = \pm 2$ as the result shown in Figure 4d (grey dashed lines). However, the obtained predication only considers the applied field $B(\mu_0 H)$ contribution, which is not consistent with the experimental data (blue and red symbols) within the error bar, proving that the contribution from induced exchange

field by $CrBr_3$ is remarkable. Most importantly, the close-up of each local R_{XX} maxima and R_{XX} minima of resistance curves taken at 2 T, 3 T and 4 T in Figure 4e reveal an anomalous resistance dip and peak-splitting features at $\nu = 0$ that develop with the increasing magnetic field, suggesting the lifting of Landau level degeneracy under large B_Z with the contribution from MPE between $CrBr_3$ and graphene. Furthermore, we observed the anomalous longitudinal resistance at the Dirac point $R_{XX,D}$ with increasing magnetic field (Figure S1, Supporting Information), which results from the MPE induced B_Z in graphene/$CrBr_3$ heterostructures, and attributes to the ground state phases of graphene transition from a ferromagnetic state to a canted antiferromagnetic state near $\nu = 0$ (Text S2, Supporting Information).

In summary, we report the investigation of MPE between monolayer graphene and 2D ferromagnet $CrBr_3$, which results in a considerable Zeeman splitting field in graphene. The MPE effect shown in our graphene/$CrBr_3$ van der Waals heterostructures therefore not only reveal the origin and prediction of magnetic exchange field at the interface of 2D van der Waals heterostructures, but also guide the design of next-generation 2D spin logic and memory devices via effect control of local spin generation and modulation.

Experimental Method Section

Device Fabrication: The natural graphite and $CrBr_3$ crystals were purchased from HQ graphene. First, a monolayer graphene sheet was exfoliated and transferred onto a 285 nm SiO_2/Si substrate by using conventional scotch tape mechanical exfoliation method, the thickness of monolayer graphene was identified by its optical contrast on SiO_2/Si substrate with an optical microscope and then confirmed by Raman spectroscopy. For electrical transport measurement of graphene/$CrBr_3$ van der Waals heterostructures, subsequently, we use electron-beam lithography, metal deposition and lift-off process to deposit Cr/Au electrodes (10 nm/20 nm) on the graphene layer, followed by using electron-beam lithography again and oxygen plasma etching to form Hall bar structure of graphene. Both acetone and isopropanol washing followed

by a vacuum annealing were adopted to remove the PMMA residues from graphene after contact formation and Hall bar patterning, this step is important because any residue on the graphene surface will not allow a good interface between $CrBr_3$ and graphene. Note that during the heterostructures assembly and contact processing, $CrBr_3$ is not initially stacked on graphene layer because the electrodes fabricating process (especially the electron-beam exposure, plasma etching and subsequent lift-off process) would seriously damage the $CrBr_3$. As to obtain a few $CrBr_3$ layers, the $CrBr_3$ crystal was first exfoliated onto a polydimethylsiloxane (PDMS) stamp in an inert atmosphere glove box with less than 0.1 ppm water and oxygen. Similarly, very thin $CrBr_3$ layers of different thicknesses were identified by using the optical contrast under different color filters and dark-field imaging. After that, a 10 nm thick $CrBr_3$ layer was picked up by a PDMS stamp in the glove box and transferred into the graphene Hall bar channel. Since only the clean side of $CrBr_3$ layer contacted with graphene, there is no PDMS residual issue in the heterostructures, which could be a problem of realizing magnetic proximity. Finally, the protective and insulated thin poly(methyl methacrylate) (PMMA) membrane was coated onto the $CrBr_3$/graphene/substrate to achieve our desired graphene/$CrBr_3$ van der Waals heterostructures. Here it is important to choose a $CrBr_3$ layer which fits the whole Hall bar channel to guarantee it also has good contact with graphene near the contact edges.

Electrical Measurements: Transport and magnetotransport measurements were performed in a Physical Property Measurement System (Model 6000) with temperature down to 2 K and magnetic field up to 9 T. The nonlocal and four-terminal longitudinal electrical resistances were acquired using a Keithley 2182A nanovoltmeter and a Keithley 2636B source meter with excitation current of 0.5 μA for high accurate electrical measurements. Multiple devices were prepared and measured (Figure S2-S4, Supporting Information).

Supporting Information

Supporting Information is available from the Wiley Online Library or from the author.

Acknowledgements
Special thanks to Stephan Roche for his help and informative discussion. This work was supported by Singapore NRF fellowship grant (NRF-NRFF2015-03) and NRF QEP grant, Singapore Ministry of Education (MOE2016-T2-2-077, MOE2016-T2-1-163 and MOE2016-T3-1-006 (S)), A*Star QTE programme.

Received: ((will be filled in by the editorial staff))
Revised: ((will be filled in by the editorial staff))
Published online: ((will be filled in by the editorial staff))

References:

[1] I. Žutić, J. Fabian, S. Das Sarma, *Rev. Mod. Phys*. **2004**, *76*, 323.

[2] S. Roche, J. Åkerman, B. Beschoten, J.-C. Charlier, M. Chshiev, S. Prasad Dash, B. Dlubak, J. Fabian, A. Fert, M. Guimarães, F. Guinea, I. Grigorieva, C. Schönenberger, P. Seneor, C. Stampfer, S. O. Valenzuela, X. Waintal, B. van Wees, *2D Materials* **2015**, *2*, 030202.

[3] H. Dery, H. Wu, B. Ciftcioglu, M. Huang, Y. Song, R. Kawakami, J. Shi, I. Krivorotov, I. Zutic, L. J. Sham, *IEEE Trans. Electron Devices* **2012**, *59*, 259.

[4] N. Tombros, C. Jozsa, M. Popinciuc, H. T. Jonkman, B. J. van Wees, *Nature* **2007**, *448*, 571.

[5] W. Han, K. Pi, K. M. McCreary, Y. Li, J. J. I. Wong, A. G. Swartz, R. K. Kawakami, *Phys. Rev. Lett*. **2010**, *105*, 167202.

[6] W. Han, R. K. Kawakami, M. Gmitra, J. Fabian, *Nat. Nanotechnol*. **2014**, *9*, 794.

[7] H. X. Yang, A. Hallal, D. Terrade, X. Waintal, S. Roche, M. Chshiev, *Phys. Rev. Lett*. **2013**, *110*, 046603.

[8] J. C. Leutenantsmeyer, A. A. Kaverzin, M. Wojtaszek, B. J. van Wees, *2D Materials* **2016**, *4*, 014001.

[9] Z. Qiao, W. Ren, H. Chen, L. Bellaiche, Z. Zhang, A. H. Macdonald, Q. Niu, *Phys. Rev. Lett*. **2014**, *112*, 116404.

[10] Z. Wang, C. Tang, R. Sachs, Y. Barlas, J. Shi, *Phys. Rev. Lett*. **2015**, *114*, 016603.

[11] J. B. Mendes, O. Alves Santos, L. M. Meireles, R. G. Lacerda, L. H. Vilela-Leao, F. L. Machado, R. L. Rodriguez-Suarez, A. Azevedo, S. M. Rezende, *Phys. Rev. Lett.* **2015**, *115*, 226601.

[12] P. Wei, S. Lee, F. Lemaitre, L. Pinel, D. Cutaia, W. Cha, F. Katmis, Y. Zhu, D. Heiman, J. Hone, J. S. Moodera, C. T. Chen, *Nat. Mater.* **2016**, *15*, 711.

[13] Y.-F. Wu, H.-D. Song, L. Zhang, X. Yang, Z. Ren, D. Liu, H.-C. Wu, J. Wu, J.-G. Li, Z. Jia, B. Yan, X. Wu, C.-G. Duan, G. Han, Z.-M. Liao, D. Yu, *Phys. Rev. B* **2017**, *95*, 195426.

[14] H. D. Song, Y. F. Wu, X. Yang, Z. Ren, X. Ke, M. Kurttepeli, G. V. Tendeloo, D. Liu, H. C. Wu, B. Yan, X. Wu, C. G. Duan, G. Han, Z. M. Liao, D. Yu, *Nano Lett.* **2018**, *18*, 2435.

[15] C. Gong, L. Li, Z. Li, H. Ji, A. Stern, Y. Xia, T. Cao, W. Bao, C. Wang, Y. Wang, Z. Q. Qiu, R. J. Cava, S. G. Louie, J. Xia, X. Zhang, *Nature* **2017**, *546*, 265.

[16] B. Huang, G. Clark, E. Navarro-Moratalla, D. R. Klein, R. Cheng, K. L. Seyler, D. Zhong, E. Schmidgall, M. A. McGuire, D. H. Cobden, W. Yao, D. Xiao, P. Jarillo-Herrero, X. Xu, *Nature* **2017**, *546*, 270.

[17] D. R. Klein, D. MacNeill, J. L. Lado, D. Soriano, E. Navarro-Moratalla, K. Watanabe, T. Taniguchi, S. Manni, P. Canfield, J. Fernández-Rossier, P. Jarillo-Herrero, *Science* **2018**, *360*, 1218.

[18] S. Jiang, L. Li, Z. Wang, K. F. Mak, J. Shan, *Nat. Nanotechnol.* **2018**, *13*, 549.

[19] B. Huang, G. Clark, D. R. Klein, D. MacNeill, E. Navarro-Moratalla, K. L. Seyler, N. Wilson, M. A. McGuire, D. H. Cobden, D. Xiao, W. Yao, P. Jarillo-Herrero, X. Xu, *Nat. Nanotechnol.* **2018**, *13*, 544.

[20] S. Jiang, J. Shan, K. F. Mak, *Nat. Mater.* **2018**, *17*, 406.

[21] Z. Wang, I. Gutiérrez-Lezama, N. Ubrig, M. Kroner, M. Gibertini, T. Taniguchi, K. Watanabe, A. Imamoğlu, E. Giannini, A. F. Morpurgo, *Nat. Commun.* **2018**, *9*, 2516.

[22] N. Sivadas, S. Okamoto, X. Xu, C. J. Fennie, D. Xiao, *Nano Lett.* **2018**, *18*, 7658.

[23] Y. Deng, Y. Yu, Y. Song, J. Zhang, N. Z. Wang, Z. Sun, Y. Yi, Y. Z. Wu, S. Wu, J. Zhu, J. Wang, X. H. Chen, Y. Zhang, *Nature* **2018**, *563*, 94.

[24] Z. Fei, B. Huang, P. Malinowski, W. Wang, T. Song, J. Sanchez, W. Yao, D. Xiao, X. Zhu, A. F. May, W. Wu, D. H. Cobden, J.-H. Chu, X. Xu, *Nat. Mater*. **2018**, *17*, 778.

[25] M. Bonilla, S. Kolekar, Y. Ma, H. C. Diaz, V. Kalappattil, R. Das, T. Eggers, H. R. Gutierrez, M.-H. Phan, M. Batzill, *Nat. Nanotechnol.***2018**, *13*, 289.

[26] D. R. Klein, D. MacNeill, Q. Song, D. T. Larson, S. Fang, M. Xu, R. A. Ribeiro, P. C. Canfield, E. Kaxiras, R. Comin, P. Jarillo-Herrero, *Nat. Phys*. **2019**, *15*, 1255.

[27] A. Avsar, A. Ciarrocchi, M. Pizzochero, D. Unuchek, O. V. Yazyev, A. Kis, *Nat. Nanotechnol.* **2019**, *14*, 674.

[28] K. S. Burch, D. Mandrus, J.-G. Park, *Nature* **2018**, *563*, 47.

[29] T. Song, X. Cai, M. W.-Y. Tu, X. Zhang, B. Huang, N. P. Wilson, K. L. Seyler, L. Zhu, T. Taniguchi, K. Watanabe, M. A. McGuire, D. H. Cobden, D. Xiao, W. Yao, X. Xu, *Science* **2018**, *360*, 1214.

[30] D. Zhong, K. L. Seyler, X. Linpeng, R. Cheng, N. Sivadas, B. Huang, E. Schmidgall, T. Taniguchi, K. Watanabe, M. A. McGuire, W. Yao, D. Xiao, K.-M. C. Fu, X. Xu, *Sci. Adv.* **2017**, *3*, e1603113.

[31] S. Jiang, L. Li, Z. Wang, J. Shan, K. F. Mak, *Nat. Electron.* **2019**, *2*, 159.

[32] M. Gibertini, M. Koperski, A. F. Morpurgo, K. S. Novoselov, *Nat. Nanotechnol*. **2019**, *14*, 408.

[33] C. Gong, X. Zhang, *Science* **2019**, *363*, eaav4450.

[34] T. Song, M. W.-Y. Tu, C. Carnahan, X. Cai, T. Taniguchi, K. Watanabe, M. A. McGuire, D. H. Cobden, D. Xiao, W. Yao, X. Xu, *Nano Lett.* **2019**, *19*, 915.

[35] H. H. Kim, B. Yang, T. Patel, F. Sfigakis, C. Li, S. Tian, H. Lei, A. W. Tsen, *Nano Lett.* **2018**, *18*, 4885.

[36] S. K. Behera, M. Bora, S. S. Paul Chowdhury, P. Deb, *Phys. Chem. Chem. Phys*. **2019**, *21*, 25788.

[37] B. Karpiak, A. W. Cummings, K. Zollner, M. Vila, D. Khokhriakov, A. M. Hoque, A. Dankert, P. Svedlindh, J. Fabian, S. Roche, S. P. Dash, *2D Materials* **2019**, *7*, 015026.

[38] W.-B. Zhang, Q. Qu, P. Zhu, C.-H. Lam, *J. Mater. Chem. C* **2015**, *3*, 12457.

[39] D. Ghazaryan, M. T. Greenaway, Z. Wang, V. H. Guarochico-Moreira, I. J. Vera-Marun, J. Yin, Y. Liao, S. V. Morozov, O. Kristanovski, A. I. Lichtenstein, M. I. Katsnelson, F. Withers, A. Mishchenko, L. Eaves, A. K. Geim, K. S. Novoselov, A. Misra, *Nat. Electron*. **2018**, *1*, 344.

[40] D. Shcherbakov, P. Stepanov, D. Weber, Y. Wang, J. Hu, Y. Zhu, K. Watanabe, T. Taniguchi, Z. Mao, W. Windl, J. Goldberger, M. Bockrath, C. N. Lau, *Nano Lett.* **2018**, *18*, 4214.

[41] Z. Zhang, J. Shang, C. Jiang, A. Rasmita, W. Gao, T. Yu, *Nano Lett.* **2019**, *19*, 3138.

[42] M. Abramchuk, S. Jaszewski, K. R. Metz, G. B. Osterhoudt, Y. Wang, K. S. Burch, F. Tafti, *Adv. Mater*. **2018**, *30*, 1801325.

[43] M. Kim, P. Kumaravadivel, J. Birkbeck, W. Kuang, S. G. Xu, D. G. Hopkinson, J. Knolle, P. A. McClarty, A. I. Berdyugin, M. Ben Shalom, R. V. Gorbachev, S. J. Haigh, S. Liu, J. H. Edgar, K. S. Novoselov, I. V. Grigorieva, A. K. Geim, *Nat. Electron.* **2019**, 2, 457.

[44] D. A. Abanin, S. V. Morozov, L. A. Ponomarenko, R. V. Gorbachev, A. S. Mayorov, M. I. Katsnelson, K. Watanabe, T. Taniguchi, K. S. Novoselov, L. S. Levitov, A. K. Geim, *Science* **2011**, *332*, 328.

[45] J. Renard, M. Studer, J. A. Folk, *Phys. Rev. Lett.* **2014**, *112*, 116601.

[46] D. A. Abanin, R. V. Gorbachev, K. S. Novoselov, A. K. Geim, L. S. Levitov, *Phys. Rev. Lett*. **2011**, *107*, 096601.

[47] D. A. Abanin, A. V. Shytov, L. S. Levitov, B. I. Halperin, *Phys. Rev. B* **2009**, *79*, 035304.

[48] H. Zhong, Z. Zhang, H. Xu, C. Qiu, L.-M. Peng, *AIP Adv.* **2015**, *5*, 057136.

[49] L. Li, Y. Yu, G. J. Ye, Q. Ge, X. Ou, H. Wu, D. Feng, X. H. Chen, Y. Zhang, *Nat. Nanotechnol*. **2014**, *9*, 372.

[50] C. Zhao, T. Norden, P. Zhang, P. Zhao, Y. Cheng, F. Sun, J. P. Parry, P. Taheri, J. Wang, Y. Yang, T. Scrace, K. Kang, S. Yang, G.-x. Miao, R. Sabirianov, G. Kioseoglou, W. Huang, A. Petrou, H. Zeng, *Nat. Nanotechnol*. **2017**, *12*, 757.

[51] H. H. Kim, B. Yang, S. Li, S. Jiang, C. Jin, Z. Tao, G. Nichols, F. Sfigakis, S. Zhong, C. Li, S. Tian, D. G. Cory, G.-X. Miao, J. Shan, K. F. Mak, H. Lei, K. Sun, L. Zhao, A. W. Tsen, *Proc. Natl. Acad. Sci. U. S. A.* **2019**, *116*, 11131.

[52] J. Liu, Q. Sun, Y. Kawazoe, P. Jena, *Phys. Chem. Chem. Phys*. **2016**, *18*, 8777.

[53] J. S. Moodera, T. S. Santos, T. Nagahama, *J. Phys. Condens. Matter*. **2007**, *19*, 165202.

[54] A. S. Mayorov, D. C. Elias, I. S. Mukhin, S. V. Morozov, L. A. Ponomarenko, K. S. Novoselov, A. K. Geim, R. V. Gorbachev, *Nano Lett*. **2012**, *12*, 4629.

Figures

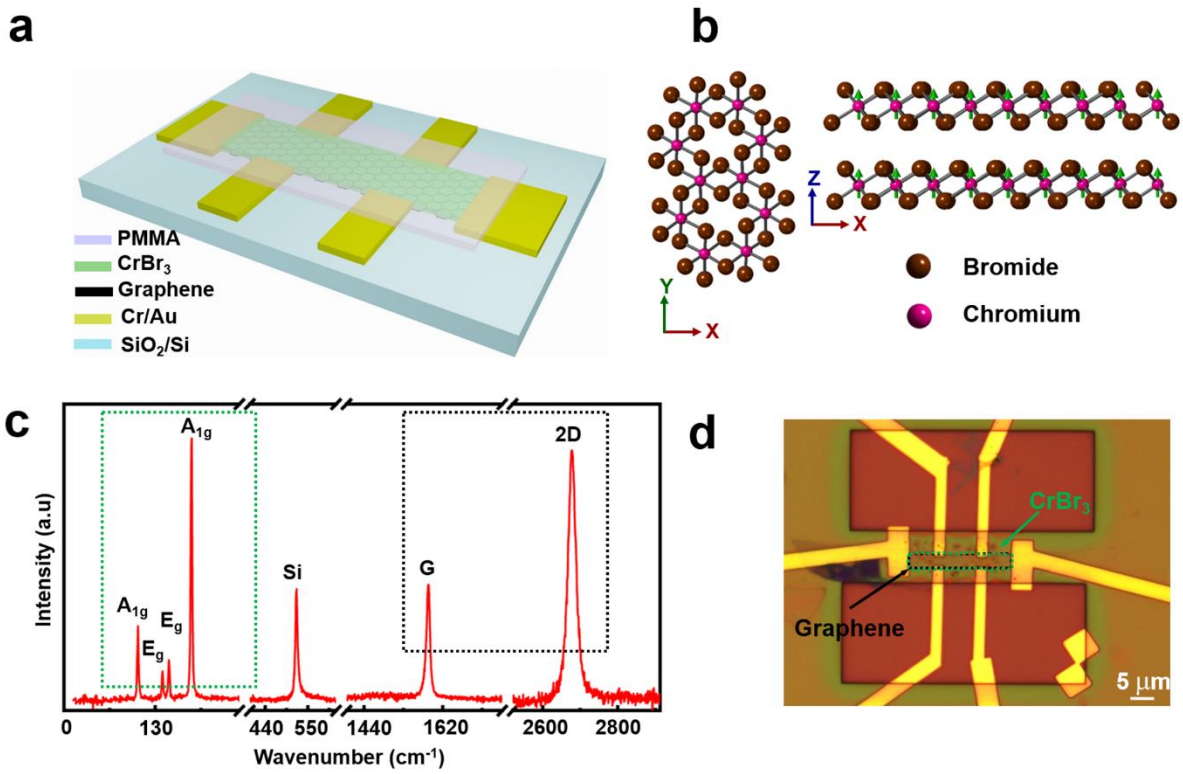

Figure 1. Fabrication and characterization of graphene/$CrBr_3$ van der Waals heterostructures. a) Scheme of graphene/$CrBr_3$ heterostructures configuration. b) Atomic structure of very thin $CrBr_3$ layers. Purple atoms: chromium; Brown atoms: bromide. Green arrow presents the spin direction of Cr^{3+} atoms. c) Raman spectrum of as-fabricated graphene/$CrBr_3$ van der Waals heterostructures without top protective cover (the black dashed area is graphene; Green dashed area is $CrBr_3$). d) Optical image of the as-prepared graphene/$CrBr_3$ heterostructures. The scale bar is 5 μm.

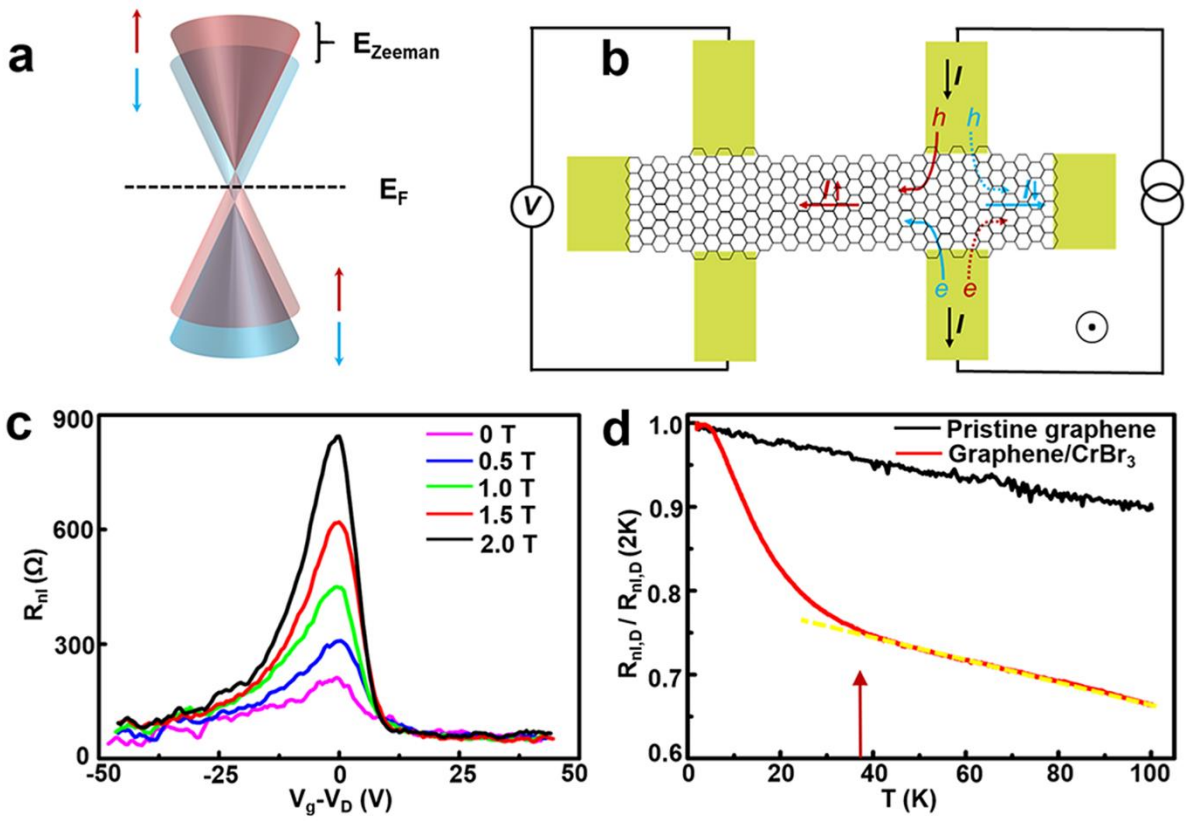

Figure 2. Zeeman spin Hall effect and non-local measurements in graphene/$CrBr_3$ heterostructures. a) Schematic diagram of Zeeman splitting of the Dirac cone in monolayer graphene (arrow represents the carrier spin direction). b) Working principle of typical non-local measurements for probing Zeeman spin Hall effect. The driven current produces transverse spin up (red) and spin down (blue) currents under an external perpendicular magnetic field, the resulting imbalance of net spin current can reach remote regions and generate a voltage drop V_{nl}. c) The non-local resistance R_{nl} as a function of the back gate V_g acquired under different external field for the graphene/$CrBr_3$ heterostructures. The sharp increase of $R_{nl,D}$(R_{nl} at Dirac point) with magnetic field suggests a strong Zeeman splitting energy enhancement. d) Temperature dependence of $R_{nl,D}$ in graphene/$CrBr_3$ heterostructures shows an abrupt slowdown as the temperature exceeds the transition temperature T_C (~37 K) of $CrBr_3$, which attributes to the $CrBr_3$'s phase change from ferromagnetic to paramagnetic state, while the $R_{nl,D}$ of pure graphene showing a very small and monotonic decrease without such perceptible onset feature. All $R_{nl,D}$ data set is taken at $\mu_0 H$ =4 T.

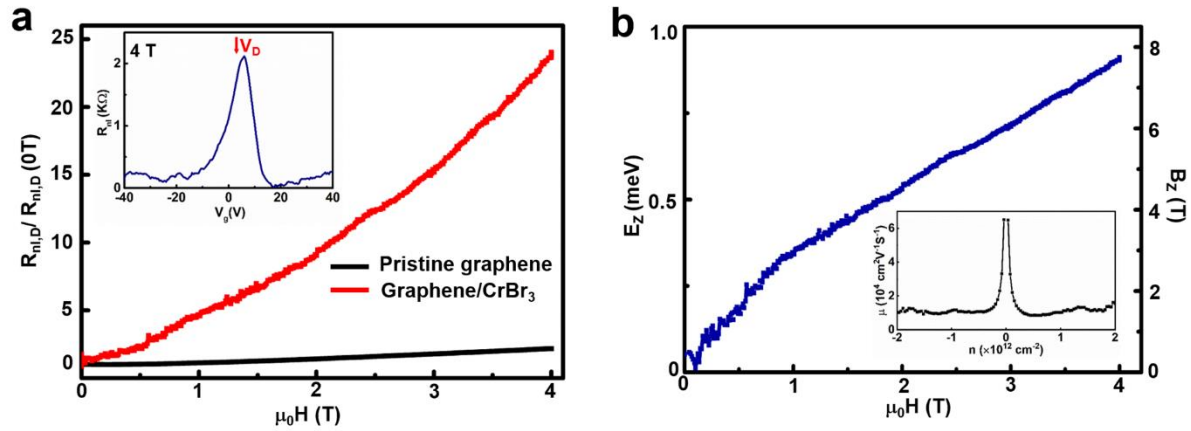

Figure 3. Magnetic field dependence measurement and the theoretical calculation of the MPE induced Zeeman splitting energy in graphene/$CrBr_3$ van der Waals heterostructures. a) The plot of $R_{nl,D}$ changes (using $R_{nl,D}$(0 T) as reference for comparison) with external magnetic field sweep measured at 2 K. It can be seen that $R_{nl,D}$ of graphene/$CrBr_3$ heterostructures rises sharply with external magnetic field increasing, reaches up to orders-of-magnitude enhancement as against pristine graphene. Inset curve is R_{nl} of graphene/$CrBr_3$ heterostructures as a function of V_g under 4 T. b) Calculated Zeeman splitting energy E_Z and corresponding Zeeman field B_Z is plotted against the external magnetic field, respectively. The inset shows field-effect mobility μ_* as a function of carrier density of graphene/$CrBr_3$ heterostructures.

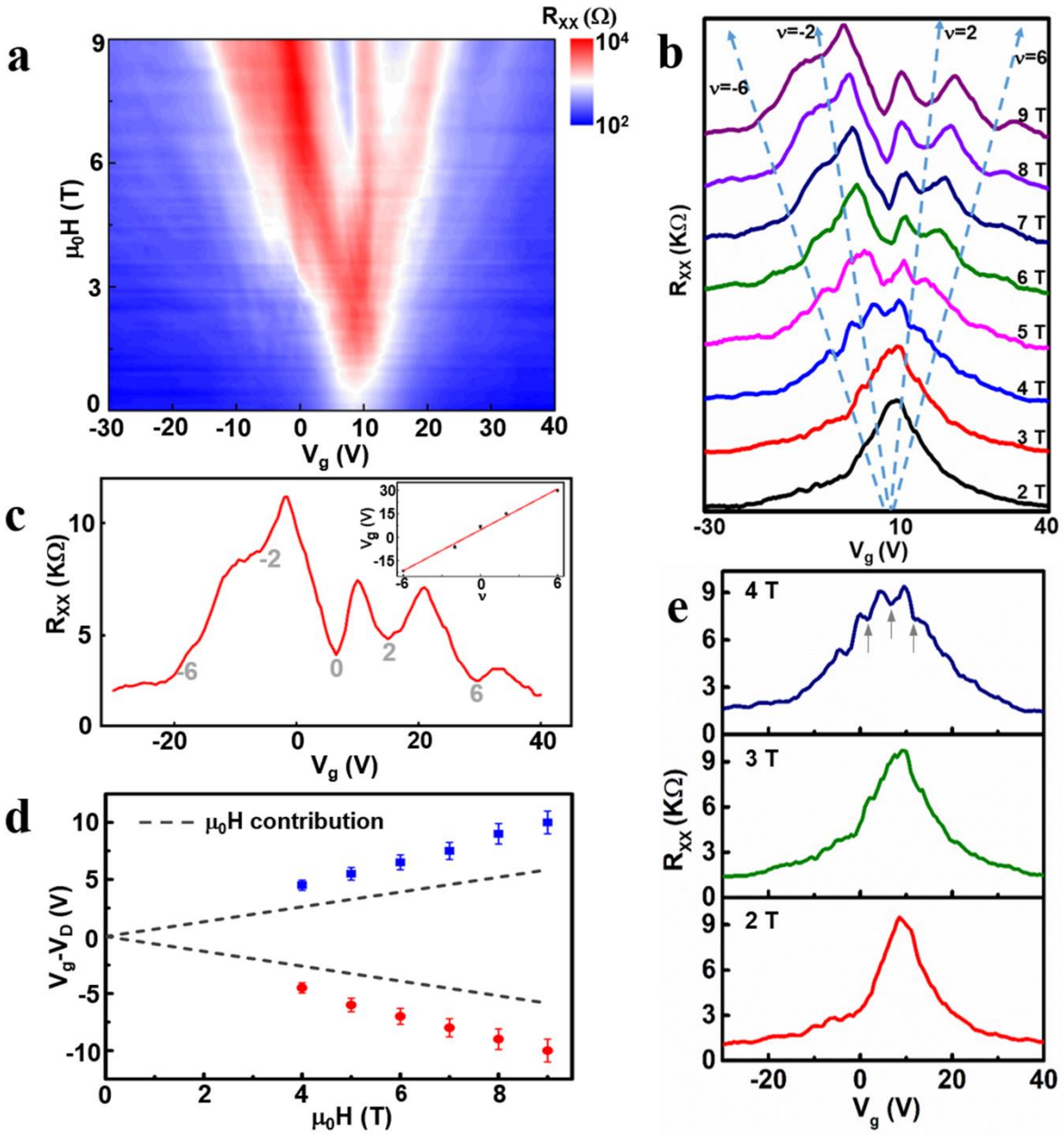

Figure 4. MPE effect in the quantum Hall regime of graphene/$CrBr_3$ heterostructures. a) Color map shows the longitudinal resistance R_{XX} as a function of the gate bias V_g and the applied magnetic field $\mu_0 H$, which is measured at 2 K. b) Extracted longitudinal resistance under external field from 2 to 9 T from (a). For clarity of labelling the Landau level filling factors, resistance curves are vertically shifted and are proportional to the applied magnetic field. c) Longitudinal resistance R_{XX} measured at 9 T shows pronounced quantum oscillations. ν is directly derived from the longitudinal resistance versus gate bias curve at each local R_{XX} minimum, and all ν are labelled in light grey. Inset figure manifests V_g is linear to each ν. d)

The theoretical predictions (dashed lines) by using capacitance model and experimental results (solid scatters with error bar) of gate bias with magnetic field at $\nu = \pm 2$. e) The close-up of each local R_{XX} maxima and R_{XX} minima of resistance curves taken at 2 T, 3 T, and 4 T, revealing an anomalous resistance dip and peak-splitting features at $\nu = 0$ that develop with the increasing magnetic field, which suggests the lifting of Landau level degeneracy under large B_Z.

The table of contents

The magnetic proximity effect (MPE) in 2D graphene/$CrBr_3$ van der Waals heterostructures is probed by Zeeman spin Hall effect via non-local transport measurements, estimation of Zeeman splitting energy demonstrates a significant magnetic proximity exchange field. The newly observed anomalous longitudinal resistances at the Dirac point with magnetic field may attribute to the new phases of ground state induced by MPE.

Keyword: magnetic proximity effect

Authors: Chaolong Tang, Zhaowei Zhang, Shen Lai, Qinghai Tan, Wei-bo Gao*

Title: Magnetic Proximity Effect in Graphene/$CrBr_3$ van der Waals Heterostructures

ToC figure:

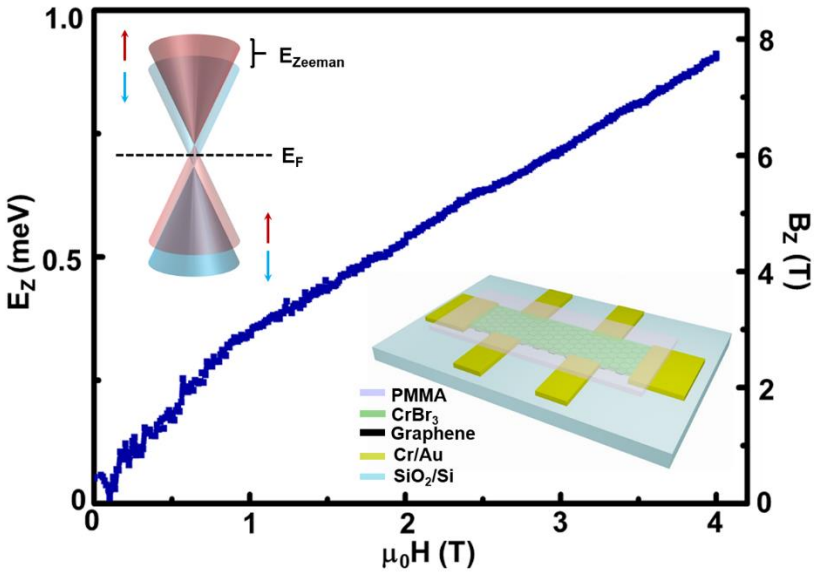

Supporting Information

Magnetic Proximity Effect in Graphene/$CrBr_3$ van der Waals Heterostructures

*Chaolong Tang, Zhaowei Zhang, Shen Lai, Qinghai Tan, Wei-bo Gao**

Dr. C. Tang, Z. Zhang, Dr. S. Lai, Dr. Q. Tan, Prof. W. Gao
Division of Physics and Applied Physics
School of Physical and Mathematical Sciences
Nanyang Technological University
Singapore 637371, Singapore
E-mail: wbgao@ntu.edu.sg

Prof. W. Gao
The Photonics Institute and Centre for Disruptive Photonic Technologies
Nanyang Technological University
Singapore 637371, Singapore

Text S1. Calculation of Zeeman splitting energy E_Z and total Zeeman field B_Z.

In pure graphene, a few publications have reported that Zeeman spin Hall effect (ZSHE) induces spin-up electrons and spin down holes due to graphene's gapless band structure, the Lorenz force further split the electron and hole states and drive this spin current perpendicular to the charge current along the Hall bar contacts[1-4]. Therefore, the ZSHE resulted from spin current can be probed by this non-local charge transport.

Theoretically, the non-local resistance predicted for the ZSHE is[1]

$$R_{nl} \equiv \frac{dV_{nl}}{dI_B} \propto \frac{1}{\rho_{xx}} \left(\frac{\partial \rho_{xy}}{\partial \mu} E_z\right)^2 \quad (1)$$

where R_{nl} is defined as the non-local resistance, V_{nl} is the non-local voltage drop between the hall bar contacts, I_B is the charge current driven across the Hall bar, μ is the chemical potential, ρ_{xx} and ρ_{xy} is the longitudinal and Hall resistivity, respectively; E_Z is the Zeeman splitting energy.

While the non-local resistance at Dirac point $R_{nl,D}$ can be further written as[1,5]

$$R_{nl,D} = R_0 + \beta(B_0) E_Z^2 \quad (2)$$

where R_0 stands for the non-local resistance at zero-field, β represents the ρ_{xx} and ρ_{xy} manifested parameters.

To directly derive the expression between E_Z and $R_{nl,D}$ at the different external magnetic field, we introduce the parameter α, which is determined by[5]

$$\alpha(B) = \sqrt{\frac{\beta(B)}{\beta(B_0)}} = \frac{E_{Z0}}{E_z} \cdot \sqrt{\frac{R_{nl,D}(B) - R_0}{R_{nl,D}(B_0) - B}} \quad (3)$$

For evaluating E_Z conveniently, we similarly choose a proper magnetic field B_0 as a reference to calculate E_Z. While β has the following form based on the given formulas above[4],

$$\beta = \frac{\omega}{2l_s} e^{-l/l_s} \frac{1}{\rho_{xx,D}} \left(\frac{\partial \rho_{xy}}{\partial \mu}\right)^2 \Big|_{\mu=\mu_D} \quad (4)$$

Where ρ_{xx} and ρ_{xy} are magnetic field dependent, other parameters are not. By considering the behavior at charge neutral point, ρ_{xx} is a sum of the Drude-Lorentz resistivity and the electron-hole drag contribution, and thus $\rho_{xx,D}$ is estimated as[2]

$$\rho_{xx,D} = \frac{m_T}{2n_T e^2 \tau}(1 + \tau^2 \Omega^2) \tag{5}$$

$$n_T = \frac{\pi}{12}\frac{K_B^2 T^2}{\hbar^2 v_0^2} \tag{6}$$

Where $m_T \approx 3.29 K_B T/v_0^2$, n_T is the density of thermally activated electrons (holes) at the charge neutral point, τ is the scattering time, and Ω is the cyclotron frequency, v_0 is Fermi velocity. By substituting β back into the parameter α, other magnetic field independent parameters are cancelled and this item is left in the form of $\sqrt{\frac{1+(\tau\Omega_{c,B_0})^2}{1+(\tau\Omega_{c,B})^2}}$ ·, which equals to $\sqrt{\frac{1+(\mu_* B_0)^2}{1+(\mu_* B)^2}}$, the mobility μ_* of the sample is about 10000 cm^2/V S in graphene/$CrBr_3$ heterostructures. As to ρ_{xy}, $\frac{\partial \rho_{xy}}{\partial \mu} = \frac{\partial \rho_{xy}}{\partial n} \cdot \frac{\partial n}{\partial \mu}$, and $\left.\frac{\partial \rho_{xy}}{\partial n}\right|_{n=0} = \frac{B}{4ecn_T^2}$, $\frac{\partial n}{\partial \mu} = \frac{2ln2}{\pi}\frac{K_B T}{\hbar^2 v_0^2}$. Finally, the parameter α can be written as

$$\alpha(B) = \sqrt{\frac{\frac{1}{\rho_{xx,D}(B)}\left(\frac{\partial \rho_{xy}(B)}{\partial \mu}\right)^2\Big|_{\mu=\mu_D}}{\frac{1}{\rho_{xx,D}(B_0)}\left(\frac{\partial \rho_{xy}(B_0)}{\partial \mu}\right)^2\Big|_{\mu=\mu_D}}} = \sqrt{\frac{1+(\tau\Omega_{c,B_0})^2}{1+(\tau\Omega_{c,B})^2}} \cdot \sqrt{\frac{\left(\frac{\partial \rho_{xy}(B)}{\partial \mu}\right)^2\Big|_{\mu=\mu_D}}{\left(\frac{\partial \rho_{xy}(B_0)}{\partial \mu}\right)^2\Big|_{\mu=\mu_D}}} = \sqrt{\frac{(1+\mu_*^2 B_0^2)B^2}{(1+\mu_*^2 B^2)B_0^2}} \tag{7}$$

$$E_Z = \frac{E_{z0}}{\alpha}\frac{\sqrt{R_{nl,D}(B)-R_0}}{\sqrt{R_{nl,D}(B_0)-R_0}} = E_{z0} \cdot \frac{\sqrt{(1+\mu_*^2 B^2)B_0^2}}{\sqrt{(1+\mu_*^2 B_0^2)B^2}} \cdot \frac{\sqrt{R_{nl,D}(B)-R_0}}{\sqrt{R_{nl,D}(B_0)-R_0}} \tag{8}$$

$$B_Z = \frac{E_Z}{g\,\mu_B} \tag{9}$$

Therefore, we could calculate E_Z and B_Z based on the deduced formula above and field dependence of $R_{nl,D}$ data in graphene/$CrBr_3$ heterostructures.

Text S2. Observed additional ground states of graphene in graphene/$CrBr_3$ heterostructures.

Another observation associated with the MPE induced B_Z is the change of anomalous longitudinal resistance at the Dirac point $R_{XX,D}$. As shown in Figure S1a, $R_{XX,D}$ initially increases with applied field until its peak at about 3 T and then drops continuously with field increasing, the behavior of which is so different with the reported monotonic increase of $R_{XX,D}$ in graphene/AlOx and other graphene heterostructures[6-8]. While the MPE effect mainly affects the $\nu = 0$ states, therefore, the intriguing behavior near $\nu = 0$ is strongly related to the novel electronic structure of graphene ground state. Nevertheless, such unusual properties of graphene/$CrBr_3$ heterostructures near $\nu = 0$ can be suitably described by the spin-polarized ferromagnetic phase in quantum Hall ferromagnetism theory[9-13] as shown in Figure S1b. In detail**,** the bulk gap at the Dirac cone is dominated by the Zeeman splitting energy E_Z through the sub-Landau level of the spin-up cone and spin-down cone crossover, the sample edge state is gapless and exist counter-propagating edge channels with opposite spins, leading to decreasing $R_{XX,D}$ as agrees with our observation. After applied magnetic field exceeds 5 T, a dramatic increase of $R_{XX,D}$ occurs, indicating additional states forming at the Dirac point with increasing B_Z and suggesting an energy gap is opened. This feature is also distinct from conventional graphene samples without magnetic coupling. However, the canted antiferromagnetic phase as described in Figure S1c from quantum Hall ferromagnetism theory could appropriately explain the abnormal ground state phase transformation of graphene, stemming from the spin-polarized ferromagnetic phase to canted antiferromagnetic phase transformation occurs with the opening of an edge state gap after 5 T.

Since the ground state phases of the graphene/$CrBr_3$ heterostructures is determined by the competition between valley isospin anisotropy energy and Zeeman splitting energy: if Zeeman splitting energy is larger than the doubled valley isospin anisotropy energy, the spin-polarized ferromagnetic phase will present; if less, it will go to canted antiferromagnetic phase[9-13]. While the valley isospin anisotropy energy only relies on the applied magnetic field, Zeeman splitting

energy is attributed to the MPE induced field and the applied magnetic field. By tuning the applied magnetic field, we can switch the graphene ground state with different phase between ferromagnetic state and canted antiferromagnetic state.

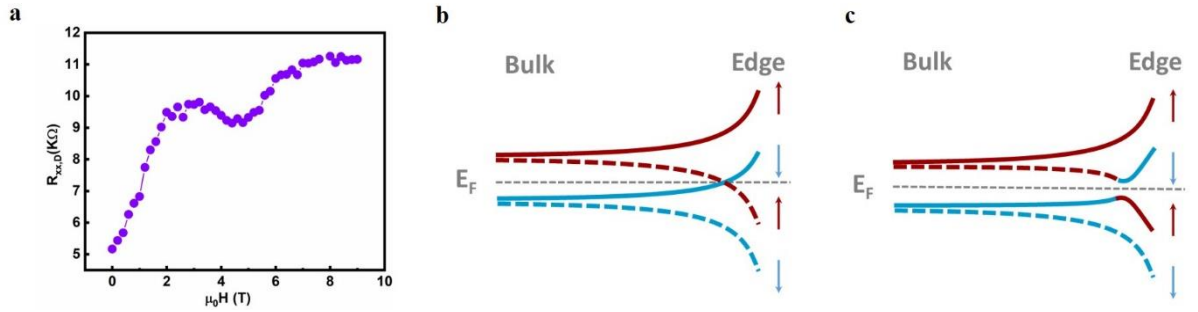

Figure S1. Ferromagnetic state to a canted antiferromagnetic state. a) longitudinal resistance at the Dirac point $R_{XX,D}$ evolves with the applied magnetic field, which initially increases to its peak with increasing magnetic field then drops continuously after 3 T. notably, $R_{XX,D}$ rises gradually again after 5 T. b) Scheme of the spin-polarized ferromagnetic phase as described in quantum Hall ferromagnetism theory. The sample edge is in gapless state and there exist counter-propagating edge channels with opposite spins, leading to decreasing $R_{XX,D}$. c) Schematic of the canted antiferromagnetic phase with the opening of an edge state gap.

Text S3. Other sample's non-local measurements

In order to verify the accuracy and repeatability of observed physics phenomenon, we fabricated and measured other samples under the same conditions. As shown in Figure S2, similarly, the non-local resistance R_{nl} at Dirac point in graphene/$CrBr_3$ heterostructures shows a huge increase as the external magnetic field goes up, confirming a distinct Zeeman splitting energy enhancement in graphene/$CrBr_3$ heterostructures.

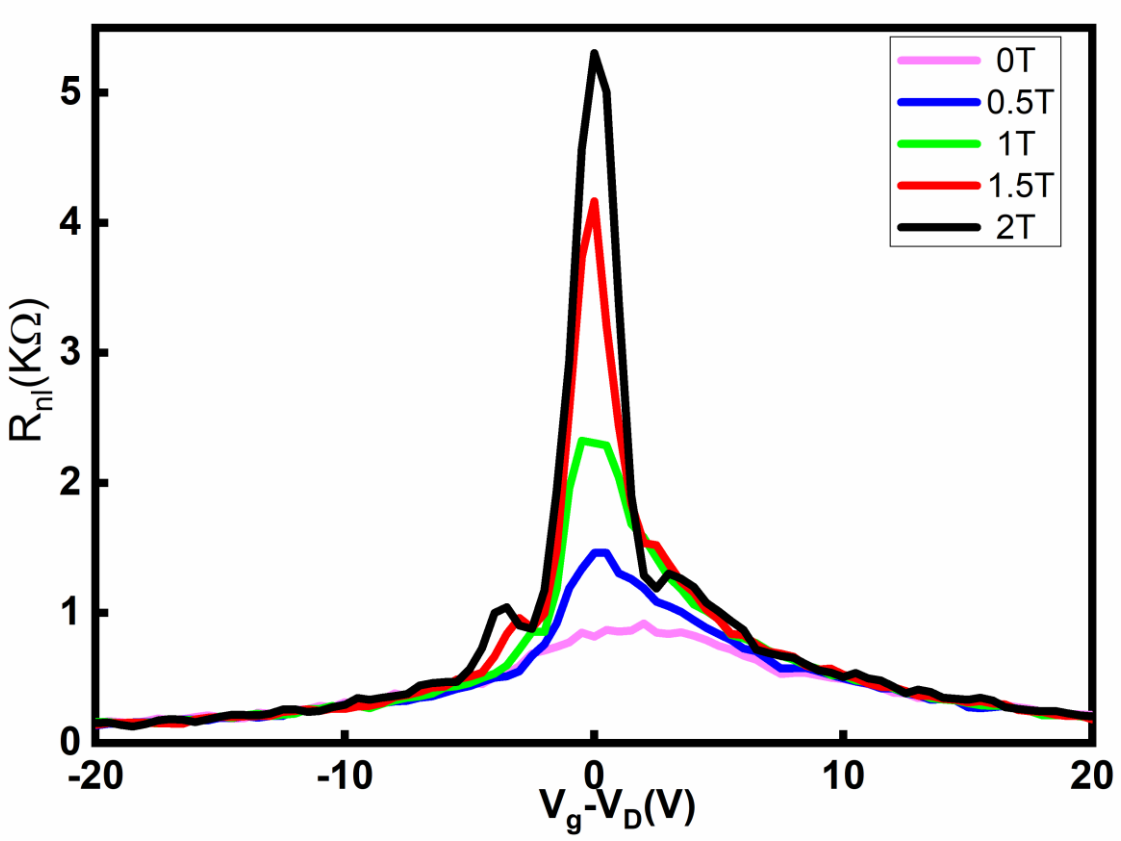

Figure S2. Non-local resistance measurement of another device with the same heterostructures and configurations.

Text S4. Other sample's four-probe longitudinal resistance measurements

As the magnetic proximity exchange field has a strong influence on the quantum state of graphene, we further examined and measured the longitudinal resistance of another sample with the same heterostructures. As shown in Figure S3, the oscillation of longitudinal resistance of graphene R_{XX} in graphene/$CrBr_3$ heterostructures is achieved at a low magnetic field. Inset shows V_g is linearly fitted to each v. Furthermore, as shown in Figure S4, the close-up of local R_{XX} minima of resistance curves taken at 2 T and 3 T reveals extra dip features (marked by red dash circle in the Figure). This peak-splitting feature usually indicates the lifting of Landau level degeneracy under large B_Z.

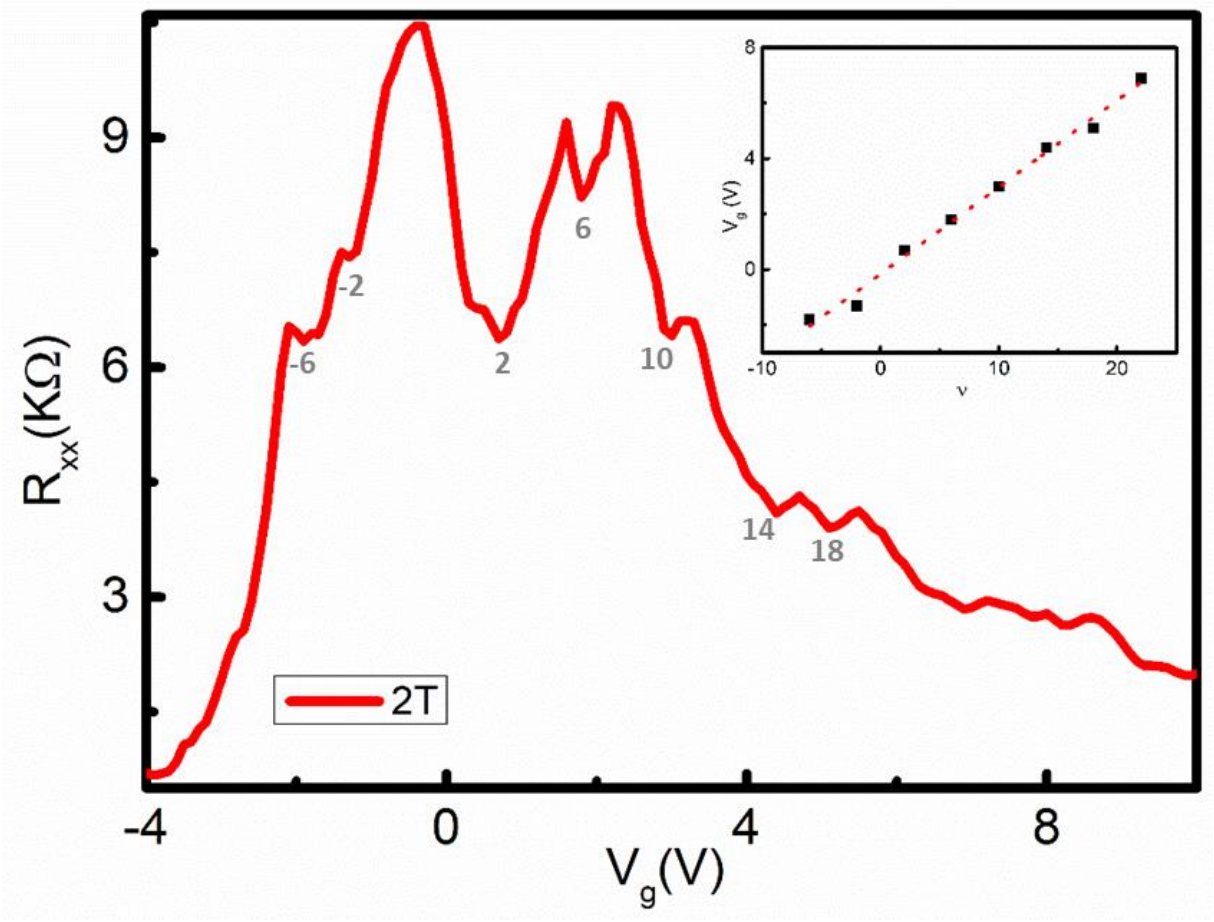

Figure S3. Oscillation of longitudinal resistance R_{XX} as a function of gate bias measured at 2 T for another device with same graphene/$CrBr_3$ heterostructures. Inset shows V_g is linear fit to each ν.

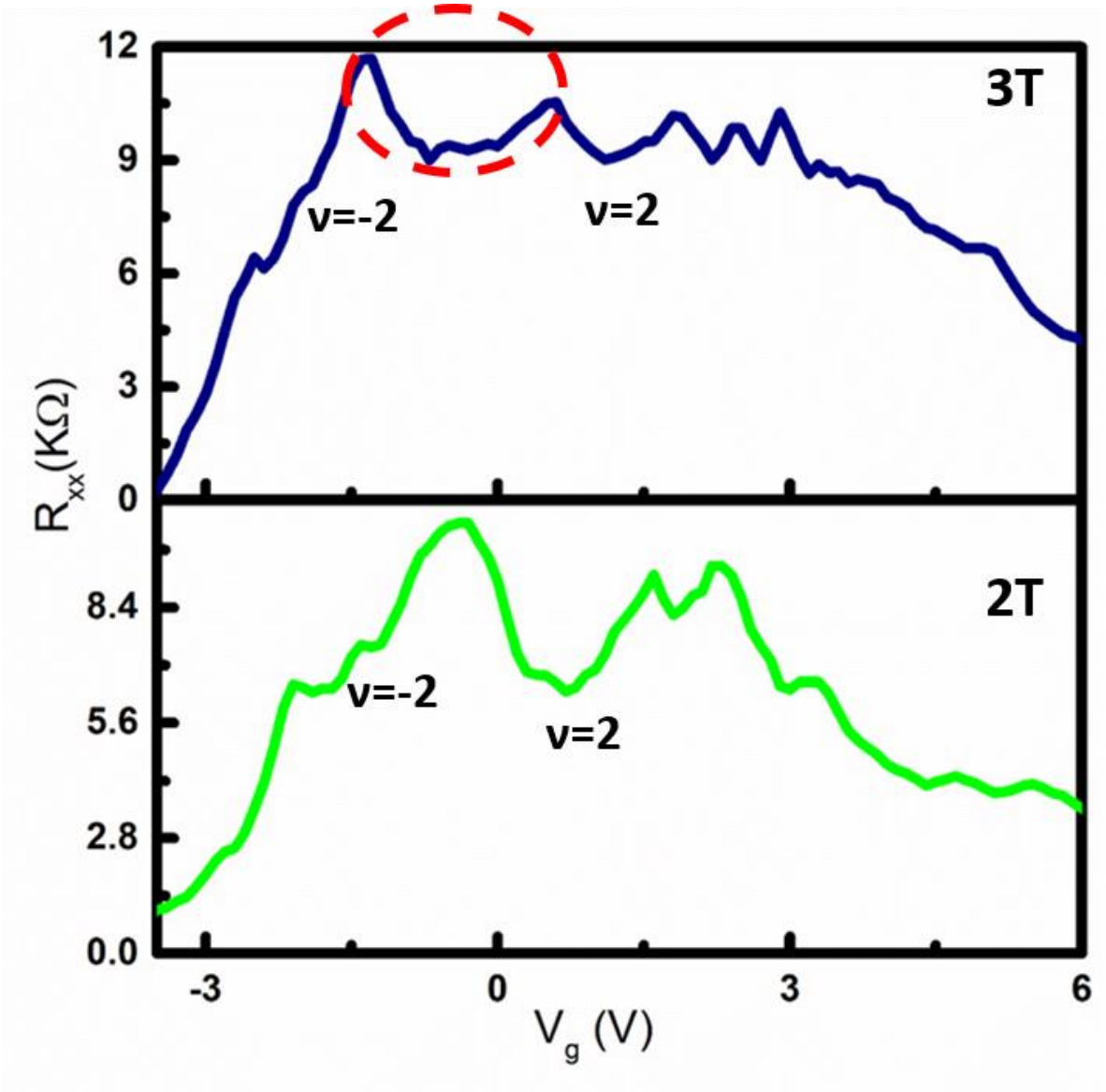

Figure S4. The close-up of local R_{XX} minima of resistance curves taken at 2 T and 3 T, revealing extra dip features which develop with the increasing magnetic field, especially near ν = 0 (marked by red dash circle in the Figure).

Text S5. **Possible sources of producing nonlocal resistance** R_{nl}

The non-local measurements in the configuration of Figure 2b may involve additional voltage signals except from ZSHE. Thus, we considered possible extrinsic sources that may contribute to R_{nl}, they are analyzed and found out to be very small comparing with ZSHE signals so as to affect entire nonlocal resistance less and can be reasonably neglected in this measurement. First,

$CrBr_3$ is an insulating ferromagnet, no electrons would prefer to go through it when coupled to a highly conductive graphene in our configuration unless in a magnetic tunnel junction design. The other considerable source to induce voltage signal in nonlocal resistance R_{nl} is the Ohmic contribution which is due to classical diffusive charge transport to the measured nonlocal resistance for a typical Hall bar structure with channel length of L and width of W. The Ohmic contribution can be further calculated by van der Pauw formula[14] $R_{nl} = \frac{\rho_{xx}}{\pi} \exp(-\pi \frac{L}{W})$, where the resistivity $\rho_{xx} = R_L \frac{W}{L}$, By using the R_{XX} data measured in Figure 4a and Hall bar geometry L/W=3.3 in Figure 1d, we compared the nonlocal resistance resulting from ohmic contribution with the measured nonlocal resistance R_{nl} in Figure S5. Obviously, the measured R_{nl}.is four orders of magnitude larger than the calculated Ohmic contribution. We therefore exclude the Ohmic contribution as the origin of the observed R_{nl}.

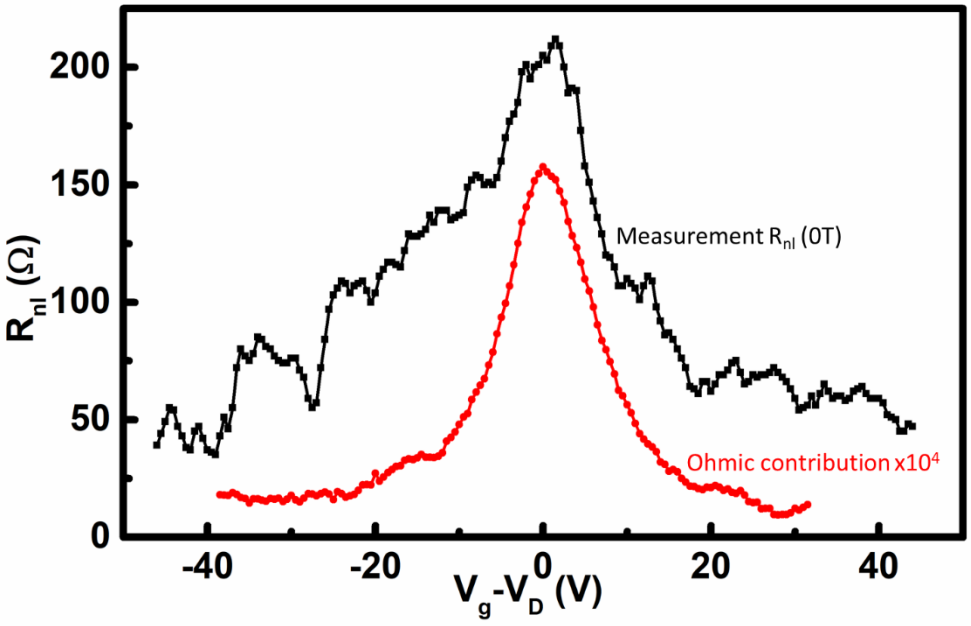

Figure S5. Comparison between the measured R_{nl} (black) and a calculation of the Ohmic contribution (magnified 10^4 times) (red). The Ohmic contribution curve is calculated using the R_{XX} data along Hall bar channel measured at 0 T.

References:

[1] J. Renard, M. Studer, J. A. Folk, *Phys. Rev. Lett.* **2014**, *112*, 116601.

[2] D. A. Abanin, R. V. Gorbachev, K. S. Novoselov, A. K. Geim, L. S. Levitov, *Phys. Rev. Lett*. **2011**, *107*, 096601.

[3] D. A. Abanin, S. V. Morozov, L. A. Ponomarenko, R. V. Gorbachev, A. S. Mayorov, M. I. Katsnelson, K. Watanabe, T. Taniguchi, K. S. Novoselov, L. S. Levitov, A. K. Geim, *Science* **2011**, *332*, 328.

[4] D. A. Abanin, A. V. Shytov, L. S. Levitov, B. I. Halperin, *Phys. Rev. B* **2009**, *79*, 035304.

[5] P. Wei, S. Lee, F. Lemaitre, L. Pinel, D. Cutaia, W. Cha, F. Katmis, Y. Zhu, D. Heiman, J. Hone, J. S. Moodera, C. T. Chen, *Nat. Mater*. **2016**, *15*, 711.

[6] Y. Zhang, Z. Jiang, J. P. Small, M. S. Purewal, Y. W. Tan, M. Fazlollahi, J. D. Chudow, J. A. Jaszczak, H. L. Stormer, P. Kim, *Phys. Rev. Lett*. **2006**, *96*, 136806.

[7] J. G. Checkelsky, L. Li, N. P. Ong, *Phys. Rev. Lett*. **2008**, *100*, 206801.

[8] F. Amet, J. R. Williams, K. Watanabe, T. Taniguchi, D. Goldhaber-Gordon, *Phys. Rev. Lett*. **2013**, *110*, 216601.

[9] M. Kharitonov, *Phys. Rev. Lett.* **2012**, *109*, 046803.

[10] A. F. Young, J. D. Sanchez-Yamagishi, B. Hunt, S. H. Choi, K. Watanabe, T. Taniguchi, R. C. Ashoori, P. Jarillo-Herrero, *Nature* **2014**, *505*, 528.

[11] M. Kharitonov, *Phys. Rev. B* **2012**, *86*, 075450.

[12] M. Kharitonov, *Phys. Rev. B* **2012**, *85*, 155439.

[13] K. Nomura, A. H. MacDonald, *Phys. Rev. Lett.* **2006**, *96*, 256602.

[14] Y. Shimazaki, M. Yamamoto, I. V. Borzenets, K. Watanabe, T. Taniguchi, S. Tarucha, *Nat. Phys*. **2015**, *11*, 1032.